applied sciences

MDPI

Article

Coseismic Slip and Downdip Afterslip Associated with the 2021 Maduo Earthquake Revealed by Sentinel-1 A/B Data

Yang He [1], Zhen Tian [2,*], Lina Su [1], Hongwu Feng [1], Wenhua Yan [1] and Yongqi Zhang [1]

[1] Shaanxi Earthquake Agency, Xi'an 710068, China; sxdzj_hy@163.com (Y.H.); sulinawhu@163.com (L.S.); gsfenghw@126.com (H.F.); yanwh0520@126.com (W.Y.); zyq19851115@163.com (Y.Z.)
[2] School of Geology Engineering and Geomatics, Chang'an University, 126 Yanta Rd., Xi'an 710054, China
* Correspondence: zhen.tian1990@hotmail.com

Abstract: On 22 May 2021, an earthquake (98.3° E and 34.59° N) struck Maduo town in Qinghai province, occurring along a relatively obscure secondary fault within the block. We utilized 105 archived Sentinel-1A/B acquisitions to investigate the coseismic deformation and the evolution of postseismic displacements in both the temporal and spatial domains, as well as the associated dynamic mechanisms of the 2021 Maduo earthquake. The interference fringes and coseismic deformation revealed that the primary feature of this event was the rupture along a left-lateral strike-slip fault. The released seismic moment was close to 1.88×10^{20} N·m, which is equivalent to an Mw 7.45 event. Simultaneously, the maximum coseismic slip reached approximately 4 m along the fault plane. The evolution of postseismic displacements in both the temporal and spatial domains over 450 days following the mainshock was further analyzed to explore the underlying physical mechanisms. Generally, the patterns of coseismic slip and afterslip were similar, although the postseismic displacements decayed rapidly over time. The modeled afterslip downdip of the coseismic rupture (at depths of 15–40 km) effectively explains the postseismic deformation, with a released moment estimated at 4.57×10^{19} N·m (corresponding to Mw 7.04). Additionally, we found that regions with high coseismic slip tend to exhibit weak seismicity, and that afterslip and aftershocks are likely driven by each other. Finally, we estimated the Coulomb Failure Stress changes (ΔCFS) triggered by both coseismic rupture and aseismic slip resulting from this event. The co- and postseismic ΔCFS show similar patterns, but the magnitude of the postseismic ΔCFS is much lower ($\leq$0.01 MPa). We found that ΔCFS notably increased on the Yushu segment of the Garze-Yushu-Xianshuihe Fault (GYXF), as well as the Maqin–Maqu and Tuosuo Lake sections of the East Kunlun Fault (EKF). Therefore, we infer that these fault segments may have a higher potential seismic risk and should be carefully monitored in the future.

Keywords: Maduo earthquake; InSAR observations; afterslip; Coulomb Failure Stress changes

check for updates

Citation: He, Y.; Tian, Z.; Su, L.; Feng, H.; Yan, W.; Zhang, Y. Coseismic Slip and Downdip Afterslip Associated with the 2021 Maduo Earthquake Revealed by Sentinel-1 A/B Data. *Appl. Sci.* **2024**, *14*, 6771. https://doi.org/10.3390/app14156771

Academic Editor: Michele Placido Antonio Gatto

Received: 6 July 2024
Revised: 29 July 2024
Accepted: 30 July 2024
Published: 2 August 2024

1. Introduction

On 22 May 2021, an earthquake (98.3° E and 34.59° N) struck Maduo town in Qinghai province, occurring along a relatively obscure secondary fault within the block. This seismic event reached a moment magnitude of Mw 7.4, which is the most significant event in the Chinese mainland since the 2008 Wenchuan earthquake [1–3]. Many earthquake research institutions reported that the epicenter of this event was situated in a sparsely populated area. Studies from field reconnaissance, aftershock distributions, and Interferometric Synthetic Aperture Radar (InSAR) unwrapping images from both ascending and descending orbits suggest that this event may have been caused by a sinistral strike-slip rupture along the Kunlun Pass-Jiangcuo Fault (KPJF) [4]. Previous studies have shown that this event resulted in a significant surface rupture with a length varying from 150 to 210 km [1–9] (Figure 1b).

The Bayan Har block is well-known for its strong seismicity and frequent earthquakes in the northern Tibetan Plateau. The Kunlun Fault forms the northern edge of the Bayan

Har block, while the Ganzi-Yushu-Xianshuihe Fault (GYXF) defines the southern edge of the block. Its eastern boundary is the Longmen Mountain orogenic belt, adjacent to the Sichuan Basin (Figure 1a). Since the 1990s, most earthquakes (>Mw 7) in the Chinese mainland have occurred on the boundaries of the block [10–12], except for this event, which occurred within the interior of the block. Therefore, this earthquake provides a valuable opportunity for studying intrablock faulting behavior and evaluating regional seismic risk in the future.

Space geodetic data, e.g., Global Navigation Satellite System (GNSS) and Interferometric Synthetic Aperture Radar (InSAR), have been conventional methods for investigating coseismic deformation and postseismic time series [10–14]. Field geological investigations indicate that this event occurred on the KPJF, which is characterized by a sinistral strike-slip motion [1,2]. Relocating the aftershock sequence after the mainshock suggests that the seismogenic fault exhibited an asymmetric bilateral rupture on a near-vertical fault plane and revealed a clear bifurcation geometry feature at the end of the surface trace [4,5]. Many studies reported that the peak coseismic slip ranged from 3.6 m to 9.3 m [3,7–9,15–25]. The Maqin–Maqu segment, in particular, may have a higher potential seismic risk, and should be carefully monitored in the future [8,9,15,17–19,22,23,25]. Based on the seismic data, strong-motion acceleration waveforms, and high-rate (1 Hz) GNSS observations, some studies revealed a nearly bilateral slip-pulse rupture caused by the event [17,26] and demonstrated the interactions on the stress triggering between the different asperities [15].

Compared to the coseismic deformation, postseismic displacement caused by a large earthquake usually occurs over a wider range and exhibits non-linear decay over time [13,14,27]. Space geodetic data, especially the InSAR time series with high spatio-temporal resolution, are crucial for investigating transient deformation after a strong earthquake, e.g., the Wenchuan earthquake [28,29], the Nepal earthquake [13,30–32], and the Yushu earthquake [33]. Huang et al. [28] found that a shallow afterslip effectively explained the near-field deformation caused by the Wenchuan earthquake and was inversely correlated with the coseismic slip distribution. Qu et al. [33] demonstrated that short-term afterslip associated with the Yushu earthquake likely contributed to the low-amplitude postseismic deformation observed along the main rupture zone. Some early studies on the 2021 Maduo earthquake have shown that afterslip occurs on the shallow portion of the seismogenic fault [20,21,23]. Other studies have suggested that aseismic slip is primarily concentrated beneath the coseismic rupture [22,24,25,34–36], but there are significant differences in the detailed spatial distributions. An accurate and reliable afterslip distribution is crucial for studying its spatial relationship with aftershocks and coseismic slip in this paper. Overall, the remaining controversies about the spatial distribution of afterslip further limit the assessment of potential seismic risk in the future. Additionally, understanding how to release postseismic stress is a primary objective of our study.

In this paper, based on archived Sentinel-1A/B acquisitions, we analyze the coseismic displacements and the evolution of postseismic displacements in both the temporal and spatial domains resulting from the 2021 Maduo earthquake. The coseismic slip and afterslip distributions are further inverted using a kinematic slip model. We also explore the spatial correlation and possible triggering mechanism between the coseismic slip, aftershocks, and afterslip. Finally, we calculate (ΔCFS) triggered by the coseismic rupture and afterslip following the mainshock on neighboring faults and evaluate the future seismic risk. In this study, it is reasonable to assume that afterslip is the sole mechanism driving the near-field transient displacements during the early stages after the mainshock.

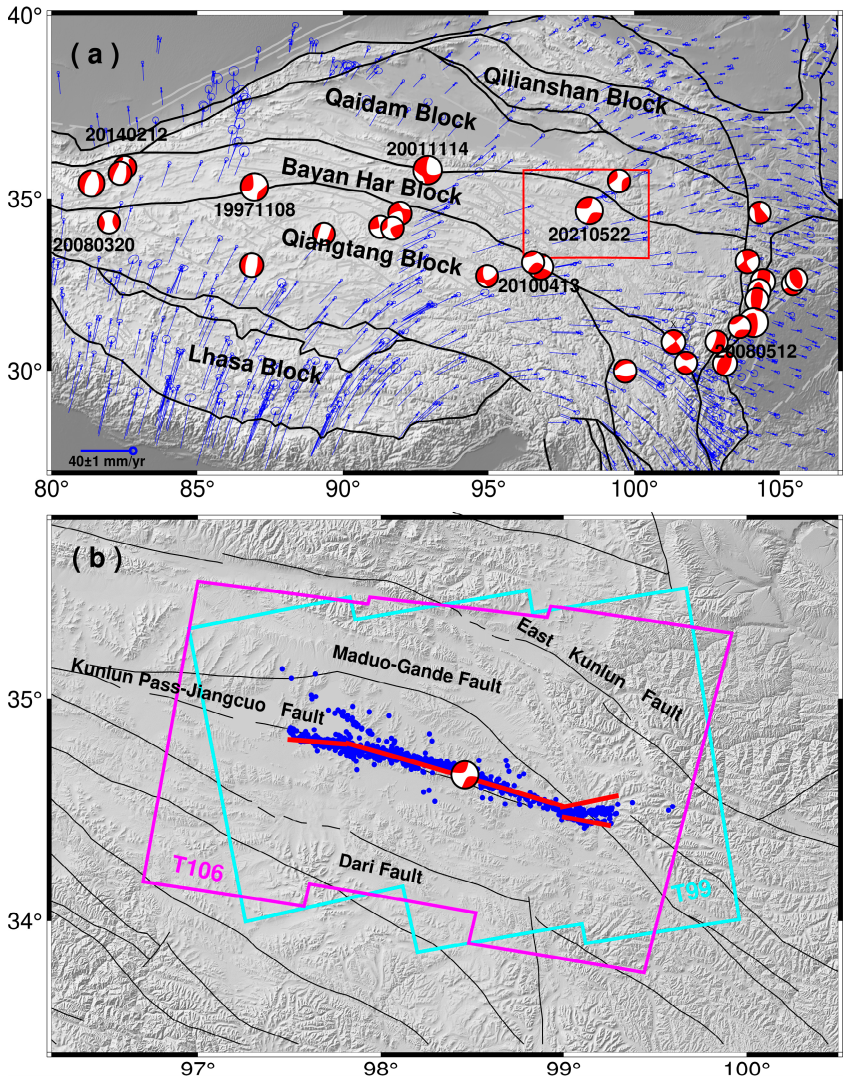

Figure 1. Tectonic setting of the study area. The blue vectors and black lines in (**a**) show the interseismic horizontal velocities [37] and block boundaries around the Tibetan Plateau, respectively. The red box in (**a**) indicates the survey region shown in (**b**). Red lines in (**b**) show the surface traces of the fault geometry [26]. The cyan and magenta rectangles in (**b**), respectively, show the ground coverage of tracks 99 and 106 images. The blue dots in (**b**) indicate the relocated aftershocks from 22 May 2021 to 30 May 2021, as referenced in Wang et al. [4]. Beach balls in (**a**,**b**) represent the focal mechanism solutions (Mw $\geq$ 6) from the Global Centroid Moment Tensor Project (GCMT, https://www.globalcmt.org/CMTsearch.html, accessed on 28 May 2024).

2. InSAR Coseismic Deformation and Postseismic Time Series

Due to the rugged topography (average elevation ~4000 m) and sparse population in the seismic region, GPS measurements are challenging. Therefore, using archived InSAR observations, we analyzed the coseismic displacements and the evolution of postseismic displacements in both the temporal and spatial domains resulting from the 2021 Maduo earthquake. The archived Sentinel-1 A/B images, which are freely available to the public, can be accessed through the Alaska Satellite Facility's official website. We utilized archived Sentinel-1 A/B acquisitions from both before and after the mainshock to retrieve the coseismic deformation (Figure 1b). To investigate the postseismic process, we also collected the Sentinel-1 A/B observations from tracks 99 and 106 for a year and a half following the mainshock. In this paper, detailed information about the archived Sentinel-1 A/B observations is presented in Table 1.

Table 1. Detailed Information about the Archived Sentinel-1 A/B Images Utilized Herein.

Usage	Date (yyyymmdd)	Track Number	Frame	Azimuth Angle (°)	Number of SAR Images
Coseismic Deformation	20210520–20210526	106	474–479	−166.97	2
	20210520–20210526	99	1290–1295	−12.89	2
Postseismic Deformation	20210526–20221205	106	474–479	−166.97	63
	20210526–20220819	99	1290–1295	−12.89	38

2.1. Coseismic Observations and Deformation

Using the differential InSAR (D-InSAR) technique, we analyzed the characteristics of coseismic deformation. The archived Sentinel-1A/B acquisitions were obtained in Terrain Observation by Progressive Scan (TOPS) mode, which requires precise co-registration. Therefore, to ensure the co-registration accuracy, we employed intensity matching and enhanced spectral diversity methods [38]. During InSAR data processing, we primarily utilized the Digital Elevation Model (DEM) to eliminate topographic phase. The Shuttle Radar Topography Mission (SRTM) DEM, acquired by the American Space Shuttle in 2000, covers 80% of the world's landmass. Additionally, NASA's publicly available 1 arc-second spatial resolution SRTM was used for further improving the co-registration accuracy of the Single Look Complex (SLC) pairs [39,40]. Before phase unwrapping based on the minimum cost flow algorithm [41], the Goldstein adaptive filtering method was applied to remove high-frequency noise [42]. Finally, we selected a multilook factor of 10:2 for the interferograms to improve the signal-to-noise ratio (SNR) [6].

Figure 2 shows that the interference fringes and coseismic displacements derived from both ascending and descending observations. The interference fringes from the ascending and descending tracks are approximately symmetrical on both sides of the surface traces. Meanwhile, for the unwrapped coseismic deformation, there are clear discrepancies along the LOS direction: the south side moves toward the descending track satellite and far away from the ascending track satellite [23], while the opposite is true for the north side. Therefore, these findings reveal that the event may be dominated by a sinistral strike-slip motion on a near-vertical fault plane [20,22,23] (Figure 2a,c). The maximum coseismic displacement in the ascending observations is approximately 0.97 m on the north of the surface traces, whereas the descending observations show about −0.79 m at the same location along the LOS direction, consistent with Zhao et al. [20]. High gradients in near-field deformation and/or serious surface damage result in phase decorrelation, suggesting that this event caused substantial destruction to the Earth's surface along the surface traces [23].

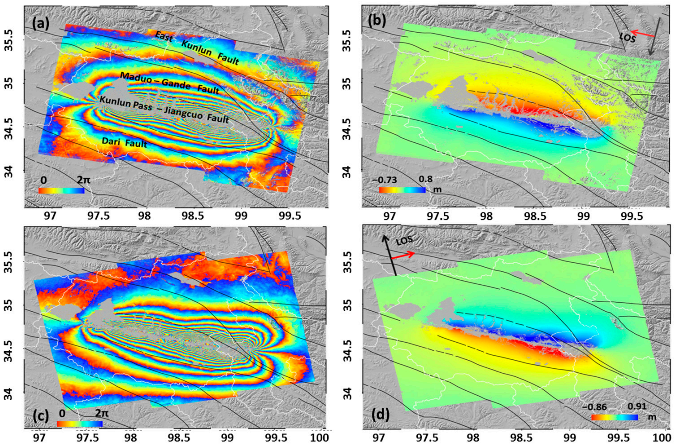

Figure 2. The original interferograms and the coseismic displacements. Bold black arrows represent the direction of the satellite's flight, while red arrows indicate the LOS directions. Panels (**a**,**b**) display the interferogram and coseismic displacements of the descending track, respectively; panels (**c**,**d**) indicate the interferogram and coseismic displacements of the ascending track, respectively.

2.2. Postseismic Observations and Time Series

Compared to coseismic deformation, postseismic deformation with relatively low amplitude is known to be difficult to observe. The transient deformation after a strong earthquake usually lasts from several months to several decades but rapidly decays over time [13,31,43]. The InSAR technique is a crucial method for studying the temporal and spatial characteristics of transient postseismic displacements resulting from this event over a 450-day period. To mitigate the phase decorrelation caused by rugged topography and dense vegetation in mountainous areas, we adopted the Persistent Scatterer InSAR (PS-InSAR) approach [44,45] to extract the postseismic time series during the 450 days following the 2021 Maduo mainshock. This was implemented by the Stanford Method for Persistent Scatterers (StaMPS version 4.1b).

The PS-InSAR approach comprehensively utilizes the phase noise and amplitude dispersion of each pixel to identify stable Persistent Scatterers (PS) points [44]. Detailed data processing procedures for the StaMPS software (version 4.1b) are shown in Appendix A. We selected a multilook factor of five looks in range and one look in azimuth for the interferograms to ensure a sufficient number of candidate PS points. Initially, we registered the slave images with a single master image and generated a series of interferograms using the GAMMA software (version 1.0-October 2014) (Figure S1). We chose the master image for the ascending orbit from 10 November 2021 and for the descending orbit from 22 November 2021. All SAR images were used, with no limitations on the temporal and spatial baselines (Figure S1). The observations were then converted into the input files required for StaMPS. Finally, we implemented a 3D phase unwrapping to derive continuous displacement using the SNAPHU algorithm [45].

During InSAR data processing, orbit errors and atmospheric anomalies have a significant impact on the extraction of the low-amplitude deformation following a large earthquake [13,31]. Therefore, the Sentinel-1 A/B precision orbit data were utilized prior to the master-to-slave image co-registration (https://dataspace.copernicus.eu, accessed on 28 May 2024). Generally, orbit error appears as a long-wavelength signal intermingled in the InSAR observations, manifesting as a phase ramp in the interferograms, which can be modeled by a quadratic polynomial [39]. Another significant error source in InSAR deformation measurement is atmospheric inhomogeneity, which results in path delay anomalies and significantly affects the accuracy of small-scale deformation observations [13]. Atmospheric anomalies consist of tropospheric and ionospheric artifacts, with tropospheric artifacts being more challenging to remove. Tropospheric artifacts can generally be divided into turbulence effects and stratification effects [46,47]. The atmospheric stratification effect on an interferogram can be mitigated by establishing the relationship between the elevation and phase delays [13,47]. In the temporal domain, the turbulence effect manifests as a high-frequency signal, while it appears as a low-frequency signal in the spatial domain. According to the spatio-temporal characteristics of turbulence, we adopt a combination of low- and high-pass filters to effectively reduce the turbulence noise [31,41]. The ionospheric artifact is primarily wavelength-dependent in this study, and its impact on C-band Sentinel-1A/B observations can generally be ignored.

The observed displacements after the 2021 Maduo earthquake may contain several signals, including linear tectonic velocities, seasonal variations due to hydrological and atmospheric loadings, and transient postseismic deformation. To extract the 'pure' postseismic time series, we first have to subtract these undesired signals. Additionally, postseismic deformation can be approximated by a logarithmic term [13,31,43], and the observed time series can be described as follows [13,40]:

$$X(t_i) = at + b \cdot \log_{10}\left(1 + \frac{t_i}{\tau}\right) + c \cdot \sin(2\pi \cdot t_i) + d \cdot \cos(2\pi \cdot t_i) + e \cdot \sin(4\pi \cdot t_i) + f \cdot \cos(4\pi \cdot t_i) \quad (1)$$

where $X(t_i)$ represents the surface observation signals after a large earthquake at the i-th time epoch (t_i), and a–f are the coefficients that need to be solved. Among them, c and d represent the annual signals, e and f represent the semiannual cycles, and τ is the decay coefficient that denotes the decay pattern of postseismic deformation. The 'pure' postseismic time series can be obtained by estimating the optimum coefficients in Equation (1) using a linear least-squares method.

Furthermore, we removed some PS points with low SNR, which are far from the fault traces, and downsampled the dataset to improve inversion efficiency. The evolution of postseismic displacements resulting from this event in both the temporal and spatial domains is shown in Figures 3 and 4. The postseismic displacements from the archived Sentinel-1A/B acquisitions on both sides of the surface traces show opposite movement directions but similar magnitudes. Compared with the coseismic displacements, the cumulative postseismic deformation has a smaller magnitude over 450 days (26 May 2021 to 19 August 2022) after the event (Figures 3 and 4). The maximum cumulative displacement from the descending observations within 450 days after this event is about 0.09 m, whereas the ascending observations show approximately −0.07 m at the same spot along the LOS direction. Therefore, on the fault plane, we reasonably assume that the transient deformation after the 2021 Maduo event may still be due to aseismic strike-slip. There are several separate and obvious near-field postseismic deformation along the rupture traces (Figure S2), implying that aseismic slip heterogeneities could exist on the seismogenic fault, and that stress release may have been segmented after the earthquake.

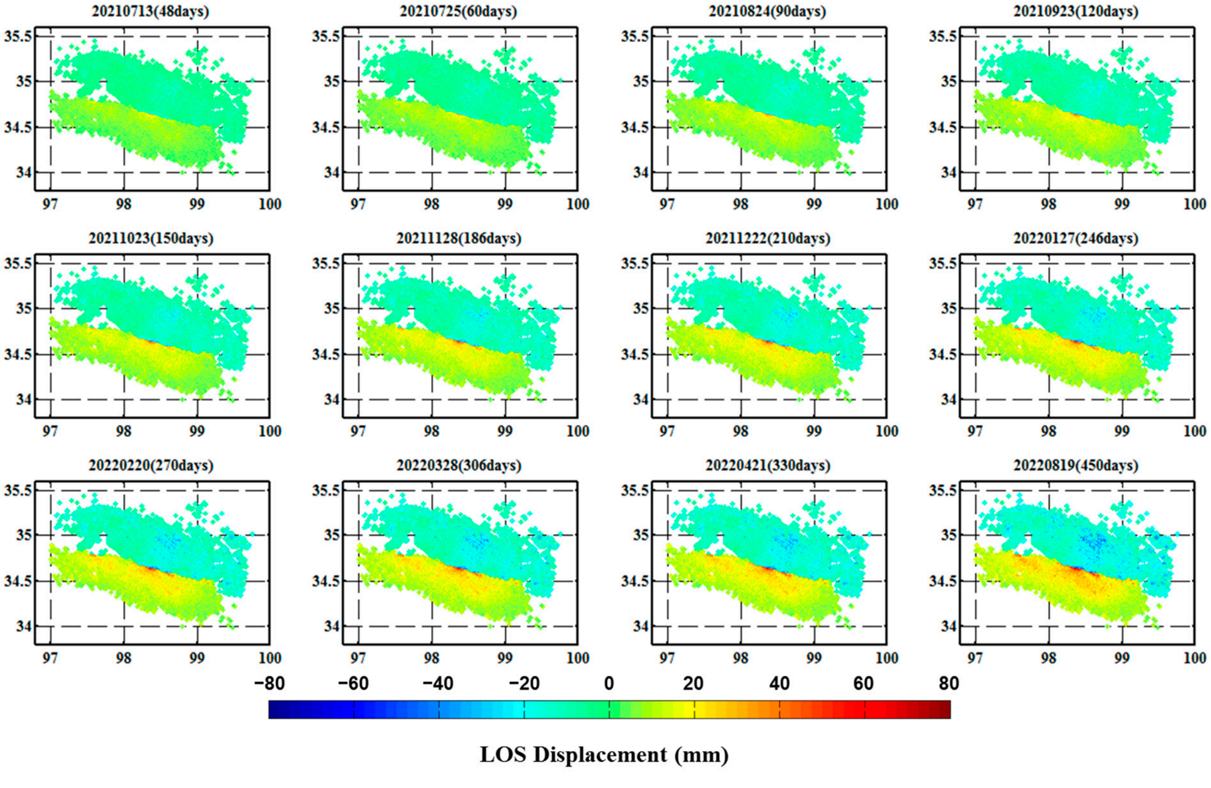

Figure 3. The InSAR time series derived from the descending track within 450 days after the mainshock.

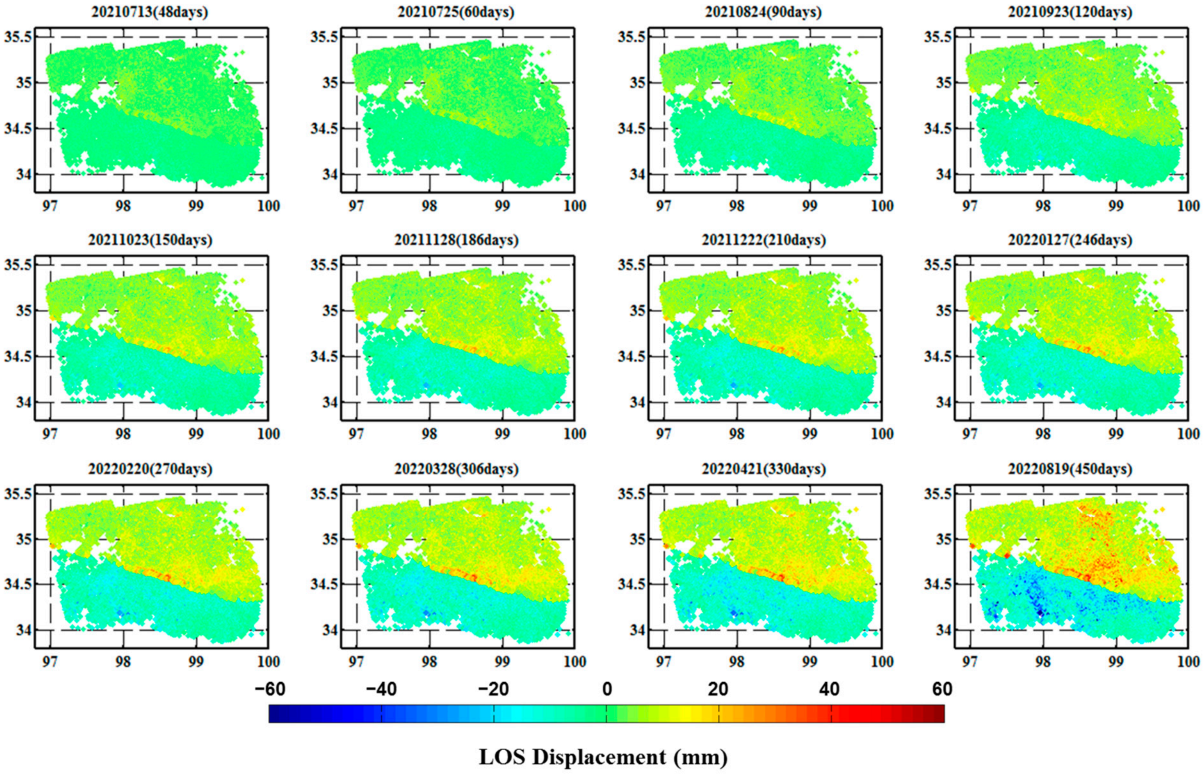

Figure 4. The InSAR time series derived from the ascending track within 450 days after the mainshock.

3. Results

Based on the coseismic deformation and postseismic time series associated with the 2021 Maduo earthquake, we built a model to invert the coseismic slip and afterslip processes. Our results indicate that the maximum coseismic slip occurs near the top of the F2 segment, east of the hypocenter, and that the postseismic deformation is well-explained by a deep afterslip. Furthermore, the above reasonable coseismic slip and afterslip results are the key to assessing the regional seismic risk.

3.1. Coseismic Model and Inversion

Using a dislocation model, we assumed the fault plane is situated in an elastic half-space and further inverted the coseismic slip distribution [48]. We utilized the study of Chen et al. [26] to set the fault parameters, dividing the fault geometry into four segments: F1 to F4 (Figure 5). F1, F2, and F3 were set to dip north with a dip angle of 80°, while F4 dips 80° toward the south. The Poisson's ratio in the model was set to 0.25. At the same time, we divided the fault plane into 5 km × 5 km sub-patches. Considering the left-lateral strike-slip characteristic of the seismogenic fault, we constrained the rake angle to vary from $-30°$ to $30°$. In order to increase inversion efficiency, the large volume of the InSAR dataset was downsampled [7]. We assigned the same weight to the ascending and descending datasets.

Based on the Steepest Descent Method (SDM), we inverted the coseismic slip derived from the archived Sentinel-1 A/B images (Figure 5) [49]. The eastern part of the seismogenic fault exhibits a larger magnitude compared to its western section, and the rupture process is also shown to propagate bilaterally along the fault [50], suggesting that it may be an asymmetric bilateral rupture event. The coseismic slip distribution is concentrated at a depth of 0–15 km, with the peak slip occurring near the surface without significant weakening [8]. The maximum coseismic slip is approximately 4 m on the F2 segment, which is identified as the main seismogenic fault segment [8,26]. Shallow slips are also concentrated in the eastern part of F1, the western part of F3, and the western part of F4. Four isolated asperities on the seismogenic fault demonstrate a complexity in frictional properties. The released seismic moment is about 1.88 × 10^{20} N·m, equating to a moment magnitude of 7.45, whereas the GCMT solution indicates a moment magnitude of 7.4. The InSAR-derived coseismic deformation may include contributions from aftershocks and early afterslip [21,22]. Based on the relocated aftershocks [4] from 22 May 2021 to 26 May 2021, the total cumulative moment released by the aftershocks is estimated to be 2.476 × 10^{17} N·m. Adding this value to the seismic moment provided by the GCMT (1.66 × 10^{20} N·m), the total moment remains significantly lower than the estimated coseismic moment in this study. That is, the overestimated seismic moment may be attributed to the early postseismic effect mixed in the coseismic InSAR observations.

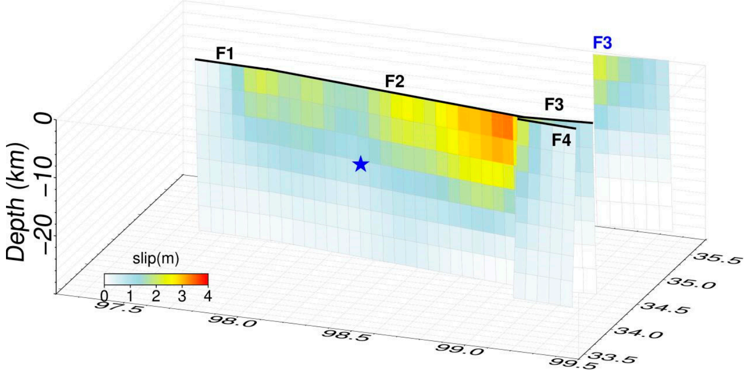

Figure 5. The coseismic slip distribution of this earthquake. This study denotes the hypocenter as a blue star.

The predicted coseismic surface displacement closely matches the actual InSAR observations (Figure 6c,f), but there are non-negligible residuals near the fault traces. These residuals may be attributed to unavoidable noise in the InSAR data processing and the potential complexity of the fault geometry or rupture process of the seismogenic fault. Refining the rupture process has always been challenging, but the inverted coseismic slip provides a means to describe the first-order features of the coseismic rupture. This contributes to further investigations into postseismic deformation mechanisms caused by coseismic stress release.

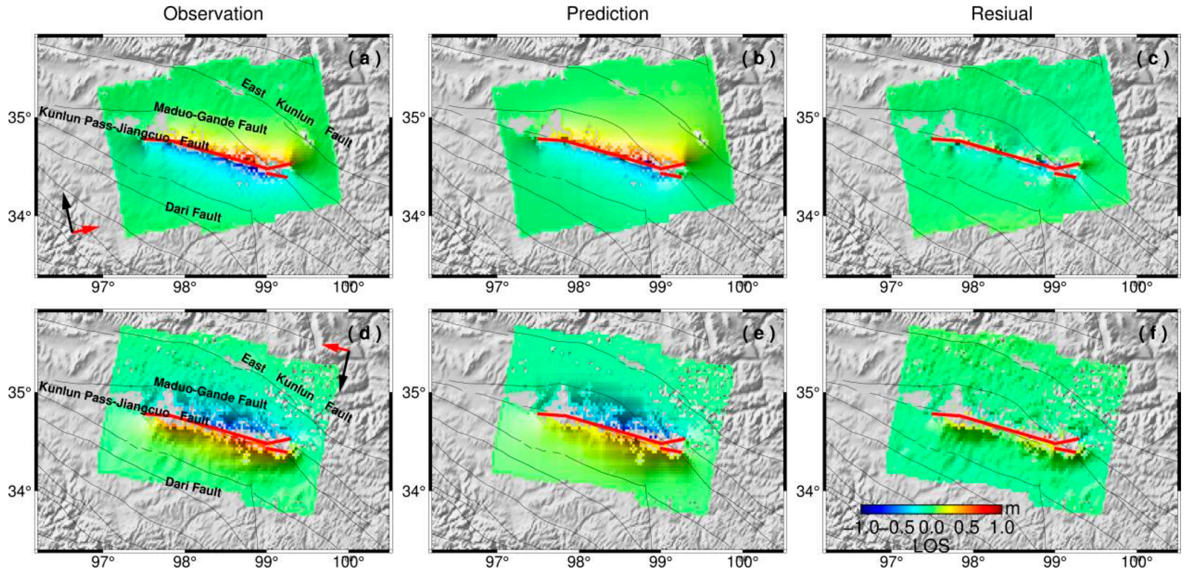

Figure 6. The coseismic displacement observations (**a**,**d**), predictions (**b**,**e**), and residuals (**c**,**f**) for tracks 99 and 106 images. Bold black arrows represent the direction of the satellite's flight, while red arrows indicate the LOS directions. The legend in (**f**) is applicable to all other figures. Red lines show the surface traces of the fault geometry.

3.2. Afterslip Model and Inversion

As mentioned above, we successfully obtained the postseismic time series from the near-field, which provides a necessary foundation for the following study. In studying the physical mechanisms following the mainshock, we typically consider three factors: afterslip, viscoelastic relaxation, and poroelastic rebound, which influence postseismic deformation either independently or jointly [43,51,52]. However, during the early stages, the near-field transient postseismic deformation is consistently driven by afterslip [22,32,43,53]. In this paper, we acquired the archived Sentinel-1A/B observations within 450 days after the mainshock, and the observed range is primarily concentrated in the near-field region, which indicates that the poroelastic rebound and viscoelastic relaxation have limited contributions to the observed displacements [35,36]. Therefore, in this study, it is reasonable to assume that afterslip is the sole mechanism driving the near-field transient displacements in the early stages following the mainshock.

We applied a fault geometry similar to the coseismic model but extended the fault to a depth of 50 km. Meanwhile, during the early stages, we further investigated the spatio-temporal evolution of afterslip following the mainshock. Our results indicate that the coseismic rupture was primarily distributed at depths of 0 to 15 km, consistent with other studies [8,18,20,26]. Previous studies found that ΔCFS triggered by the coseismic rupture is concentrated beneath the coseismic rupture [19,22,24]. This complies with the rate-strengthening conservative law. The coseismic zone is generally deemed to be a rate-weakening zone, where afterslip rarely occurs. Conversely, the zone with increasing Coulomb stress is considered a rate-strengthening zone where afterslip is generated [22,24]. Therefore, the afterslip region is constrained to depths of 15–50 km in this study.

The spatio-temporal InSAR measurements are beneficial for constraining the afterslip evolution, as shown in Figure 7. Spatially, F1 and F2 exhibit significant afterslip, while F3 and F4 show no obvious afterslip. On the segment F1, the afterslip during the 450 days following the mainshock is concentrated at depths between 20 and 35 km, with a maximum slip of approximately 0.3 m. On Segment F2, the afterslip during the same period occurs at depths ranging from 15 to 40 km, with a maximum slip of approximately 0.47 m. The released moment due to the afterslip reaches 4.57 × 10^{19} N·m, corresponding to an Mw 7.04. Given that the time period of the InSAR data we used is similar to that used by Shu et al., the released moment in our study shows slight differences compared to their findings [35]. The model predictions in the ascending and descending orbits also fit the observations well as shown in Figure 8.

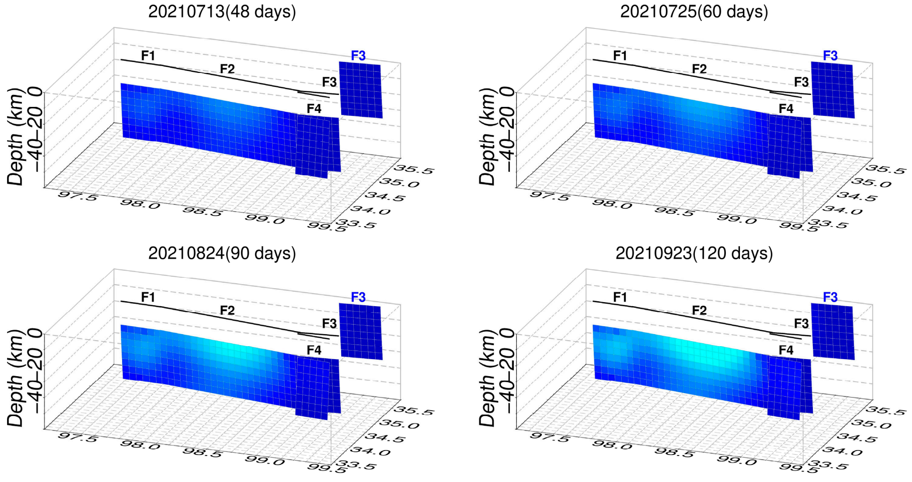
20210713(48 days)
20210725(60 days)
20210824(90 days)
20210923(120 days)

Figure 7. *Cont.*

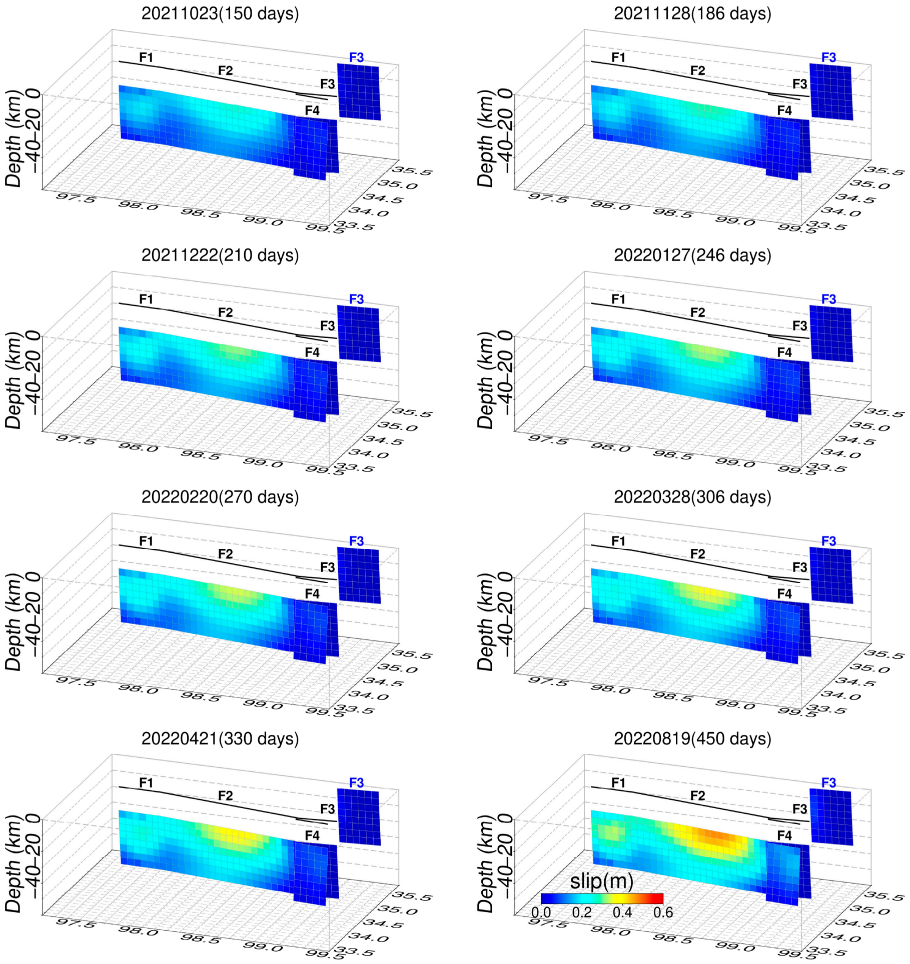

Figure 7. The spatio-temporal evolution of afterslip on the fault plane (F1–F4) corresponds to the 12 snapshots of the InSAR observations in Figures 4 and 5. Each panel title denotes the observation time (in accumulated days) after this event. The legend is applicable to all other figures.

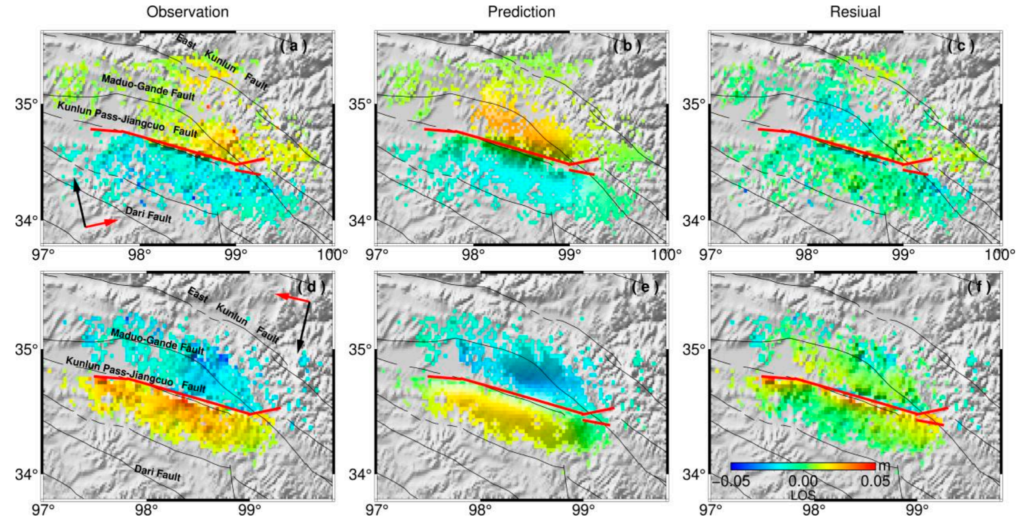

Figure 8. The postseismic displacement observations (**a**,**d**), predictions (**b**,**e**), and residuals (**c**,**f**) for tracks 99 and 106 images over 450 days after this event. The red lines in (**b**) show the surface traces of the fault geometry. Bold black arrows represent the direction of the satellite's flight, while red arrows indicate the LOS directions. The legend in (**f**) is applicable to all other figures. Red lines show the surface traces of the fault geometry.

4. Discussion

4.1. Decay Pattern of the Postseismic Displacements

Using the InSAR time series, we selected four points on both sides of the fault traces (detailed description in Figure S2) to illustrate the decay pattern of postseismic transient deformation over time. The postseismic displacements from the InSAR observations increase over time at these selected sites, but rapidly decay in the early days (Figures 9 and 10). We then separately fitted the time series to estimate the optimum decay coefficient (τ). In this paper, our results show that the decay coefficients are different at these four sites. Compared with the far-field region, the optimum decay coefficient (τ) is smaller at the near-field points, that is, near-field transient postseismic deformation decays more rapidly. The optimal decay coefficients τ for tracks 99 and 106 images were, respectively, 132 and 46 days. Compared to ascending data, descending orbit data have shorter sampling intervals and longer observation times in the early stages, resulting in a smaller decay coefficient. Similarly, for the Nepal event, Zhao et al. [30] estimated the optimal $\tau = 30$ days, while Tian et al. [43] proposed an optimal decay coefficient close to 83 days by the similar method. This discrepancy might be due to the different time windows.

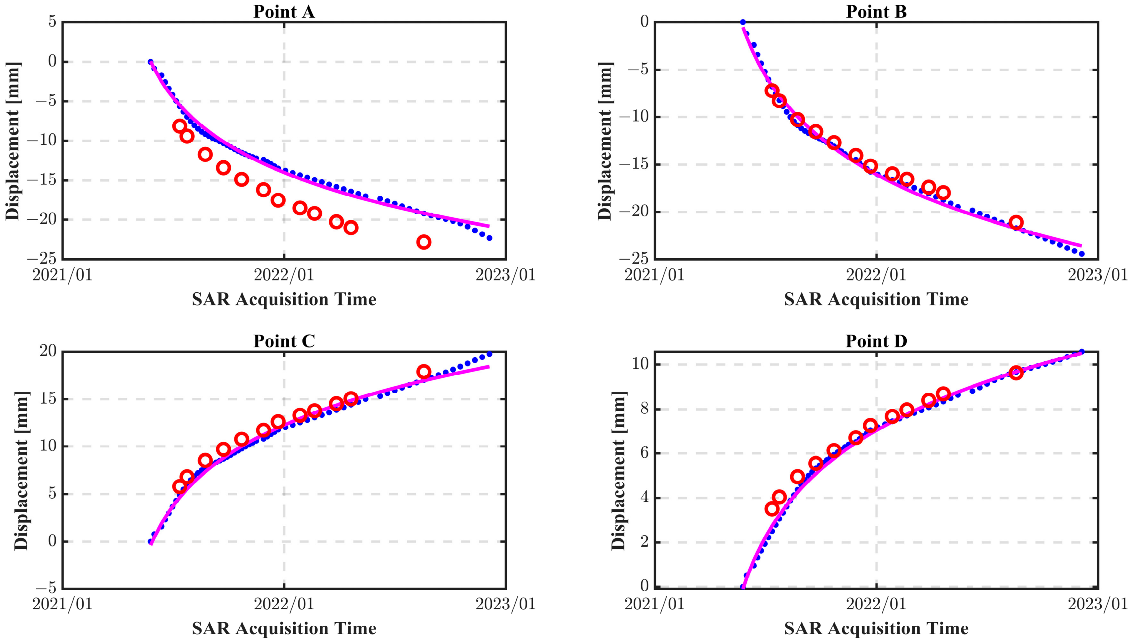

Figure 9. The postseismic time series from the descending track at four selected sites. The blue points denote the InSAR time series without seasonal signals. The red circles represent the surface deformation simulated by the afterslip model, corresponding to the 12 snapshots in Figure 7. The pink curves show the postseismic time series fitted by the logarithmic equation.

We further estimated the residuals between the actual InSAR observations and the postseismic deformation predictions from the afterslip model. Our study found that the average RMS for tracks 99 and 106 images is less than 5 mm at the four selected sites, which suggests that early postseismic deformation is likely dominated by the downdip afterslip. However, a non-negligible discrepancy exists between the model predictions and observations at point A, which may be due to the unavoidable noise in the InSAR observations or other postseismic mechanisms, such as viscoelastic relaxation.

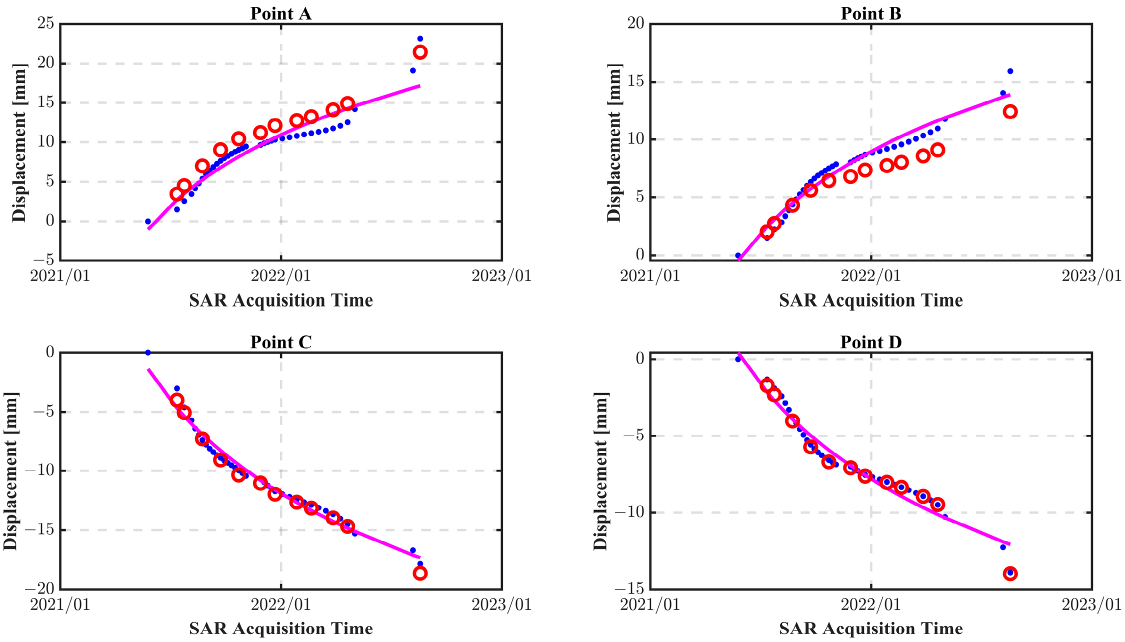

Figure 10. The postseismic time series from the ascending track at four selected sites. The blue points denote the InSAR time series without seasonal signals. The red circles represent the surface deformation simulated by the afterslip model, corresponding to the 12 snapshots in Figure 7. The pink curves show the postseismic time series fitted by the logarithmic equation.

4.2. Spatial Relationship between Coseismic Slip, Afterslip, and Aftershocks

The relocated aftershocks from 22 May 2021 to 30 May 2021, as referenced in Wang et al. [4], are concentrated at depths of 8–13 km. For ease of visual comparison, we counted the number of aftershocks along the strike at 5 km intervals, as shown in Figure 11. We found that aftershocks rarely occur in the region of high coseismic slip between 98.6° E and 99° E (only 114 events, accounting for 9.4%). However, 377 aftershocks (accounting for 31.2%) are concentrated between 98.2° E and 98.6° E. In this area, the maximum coseismic slip is about 1.8 m, significantly lower than the peak slip in the eastern region, that is, regions with high coseismic slip tend to exhibit weak aftershock activity, which can be interpreted as the heterogeneous stress release from interseismic asperities on the fault plane. The area with peak slip represents a higher amount of coseismic stress release, leading to insufficient residual stress to trigger subsequent aftershocks. Conversely, areas with lower coseismic slip, but close to the peak rupture area, may have the potential to produce aftershocks. Shu et al. [34] also reached similar conclusions, indicating that aftershocks predominantly occur in regions with lower coseismic slip. This phenomenon may be further connected to interseismic accumulated strain and the heterogeneous frictional properties on the seismogenic fault, similar to the result found in the Maule earthquake of 2010 [54].

The afterslip due to the 2021 Maduo earthquake mainly occurred at depths of 15–40 km on the segments F1 and F2, which is close to the area with increased Coulomb stress estimated by previous studies [22,24]. The coseismic rupture is generally considered to be a rate-weakening nucleation zone, while afterslip typically occurs in the rate-strengthening zones. Huang et al. [28] found that shallow afterslip resulting from the 2008 Wenchuan earthquake was inversely correlated with the coseismic slip distribution. Therefore, the afterslip is constrained to the downdip area of the coseismic rupture [19,22,24]. The cumulative afterslip during the 450 days following the mainshock is concentrated on the segment F2, ranging from 98.2° E to 98.8° E at depths of 15–40 km, with a maximum slip of approximately 0.47 m. However, Shu et al. [35] found that the peak slip is located to the west of the hypocenter. On the segment F1, afterslip ranges from 97.5° E to 97.8° E at depths of 20–35 km, with a maximum slip of 0.3 m, which is deeper than the results reported by Shu et al. [35]. The discrepancy in afterslip distributions on the different fault segments further reveals the inhomogeneous frictional properties [25].

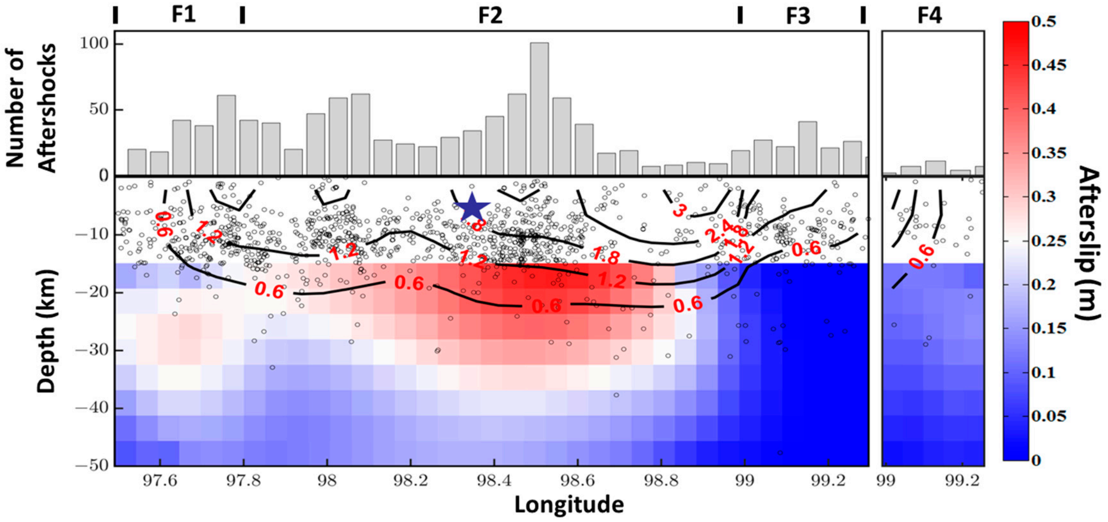

Figure 11. On the fault plane, we present spatial distribution of coseismic slip, aftershocks, and afterslip with respect to depth. Black circles represent aftershocks. The hypocenter is represented by a blue star. The black contours show the coseismic slip at 0.6 m intervals. The histogram shows the number of aftershocks along the strike at 5 km intervals. The colored rectangles indicate the cumulative afterslip during the 450 days after the earthquake.

In addition, the distribution characteristics of deep afterslip along the strike are quite similar to those of shallow aftershocks, particularly in the range of 98° E–98.8° E. In this region, there is a higher number of aftershocks corresponding to the areas of concentrated afterslip (Figure 11). We also found that the number of aftershocks along the strike exhibits semi-logarithmic migration over time (Figure S3). This spatial relationship between afterslip and aftershocks was also observed in the 2015 Mw 7.8 Pedernales (Ecuador) earthquake, suggesting that afterslip and aftershocks potentially drive each other [55]. However, the relocated aftershocks were collected during the first 8 days after the mainshock. The driving relationship between aftershocks and afterslip still needs to be verified by additional observations, such as continuous GPS and more seismic data in the future.

4.3. The Effects of Coulomb Failure Stress Triggered by Coseismic Rupture and Aseismic Slip on Surrounding Faults

The large earthquakes can be viewed as a release of interseismically accumulated stress, inevitably causing stress disturbances and redistribution in the surrounding crustal medium. We then estimated the Coulomb Failure Stress changes (ΔCFS) to evaluate seismic risk on adjacent faults as follows [56,57]:

$$\Delta \mathrm{CFS} = \Delta\tau + \mu' \Delta\sigma_n \tag{2}$$

ΔCFS is the change in Coulomb stress on the receiver fault, $\Delta\tau$ is the change in shear stress, μ' represents the effective friction coefficient, and $\Delta\sigma_n$ is the change in normal stress.

An increase in Coulomb stress of 0.01 MPa on the fault is typically regarded as the threshold to trigger a rupture [57]. We used the PSGRN/PSCMP codes to calculate the ΔCFS triggered by the coseismic rupture and afterslip on the surrounding major faults due to this event [58]. In this study, the Crust 2.0 model was used to set up a multi-layered lithospheric model. Additionally, on the fault plane, our study set the effective friction coefficient to 0.4 [15,16,57]. The coseismic ΔCFS notably increased on the Yushu segment in the GYXF, as well as the Tuosuo Lake segment and the Maqin–Maqu segment in the EKF, exceeding the threshold of 0.01 MPa (Figure 12a), consistent with previous studies [23,57,58]. The western Dari Fault (DF) also experienced a notable ΔCFS increase, which slightly differs from the results of Li et al. [57]. This discrepancy may be due to the different coseismic slip models used by Li et al. [57] and in our study.

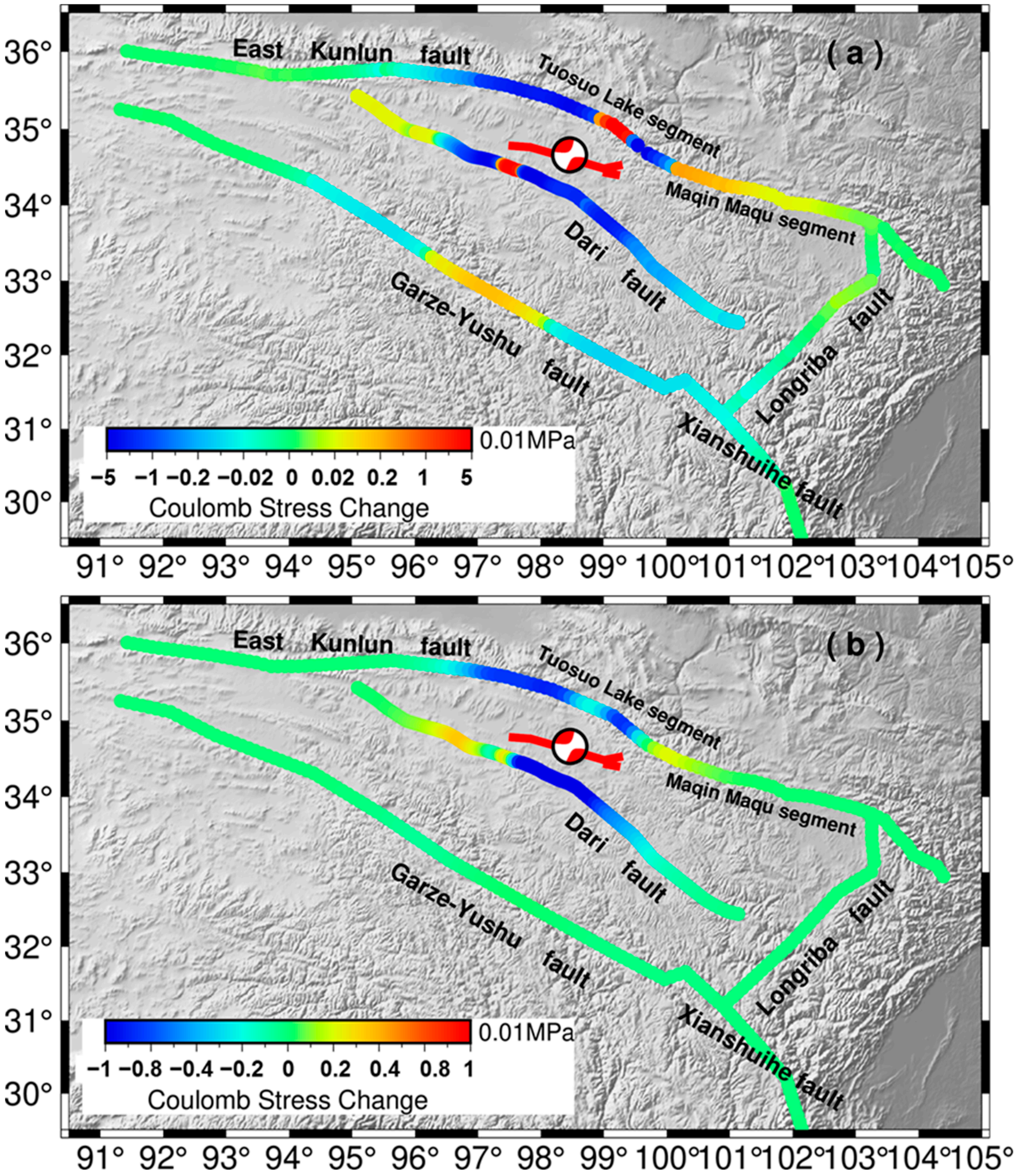

Figure 12. (**a**) The coseismic ΔCFS caused by the event. (**b**) The postseismic ΔCFS caused by the afterslip during the 450 days following the mainshock. The surface traces of the fault geometry are represented as the bold red lines and are shown in (**a**,**b**). Beach balls represent the focal mechanism solutions related to the 2021 Maduo event.

In this paper, the ΔCFS triggered by afterslip was also estimated on the surrounding faults during the 450 days following the mainshock (Figure 12b). In general, The co- and postseismic ΔCFS show a similar pattern, but the magnitude of the postseismic ΔCFS is much lower (<0.01 MPa). The postseismic ΔCFS is increased to 0.002 MPa on the Maqin–Maqu segment in the EKF and to 0.003 MPa on the western part of the DF. However, the postseismic

ΔCFS decreased on the western Tuosuo Lake segment in the EKF and the southeast of the DF [23]. On the Yushu segment in the GYXF, afterslip did not cause the obvious changes in Coulomb stress during the 450 days after the mainshock.

Previous studies have suggested there is a seismic gap on the Maqin–Maqu segment in the EKF [20,41]. The study of Li et al. [59] indicated that on the Maqin segment, the elapsed time since the most recent seismic event is approximately 400 years, approaching the most recent paleoseismic recurrence cycle of 600 ± 100 years; meanwhile, on the Maqu segment, the elapsed time is about 1000 years, significantly exceeding the latest recurrence interval of 650 ± 150 years. Additionally, on the Maqin–Maqu segment, some large earthquakes around or within the Bayan Har block could impose stress loadings e.g., the Wenchuan earthquake, the Kokoxili earthquake, and the Jiuzhaigou earthquake, [10,60]. Zhu et al. [38] also found that most parts of the Maqin–Maqu Fault are fully locked based on interseismic InSAR observations, leading to multiple asperities on the fault plane. Our study also suggests that the coseismic ΔCFS increased significantly on the Maqin–Maqu section, exceeding the triggering threshold [8,9,15,17–19,22,23,25]. Therefore, the Maqin–Maqu section may have a higher potential seismic risk and should be carefully monitored in the future.

5. Conclusions

We collected 105 archived Sentinel-1 A/B observations to extract the coseismic deformation and analyze the evolution of postseismic displacements resulting from the 2021 Maduo earthquake in both the temporal and spatial domains. Additionally, the spatio-temporal evolution of the afterslip was further modeled. The coseismic and aseismic slip distributions reveal the heterogeneous frictional properties of the seismogenic fault. Our study suggests that the afterslip primarily occurs downdip of the coseismic rupture at depths of 15–40 km, with the maximum aseismic slip occurring to the west of the peak coseismic slip. We also found that regions with high coseismic slip tend to exhibit weak seismicity. Additionally, the deep afterslip shows a similar pattern to the shallow aftershocks, suggesting that the afterslip and aftershocks are likely driven by each other. This study successfully constrained the afterslip process induced by the Maduo earthquake using InSAR observations, suggesting a possible interaction between afterslip and aftershocks. This provides a novel perspective for understanding the postseismic stress release process. Moreover, the coseismic stress significantly increases on the Yushu segment in the GYXF, as well as the Maqin–Maqu segment and the Tuosuo Lake segment in the EKF. Therefore, the Maqin–Maqu segment is considered an important seismic gap with a higher degree of fault locking. Consequently, the Maqin–Maqu segment may have a higher potential seismic risk and should be carefully monitored in the future. Additionally, more in-depth studies on the postseismic mechanisms of the Maduo earthquake can be conducted by combining longer-term InSAR data with GNSS data, and the rheological mechanisms of the region can be further analyzed using geophysical exploration methods.

Supplementary Materials: The following supporting information can be downloaded at: https://www.mdpi.com/article/10.3390/app14156771/s1, Figure S1: Distribution of temporal and spatial baselines of the interferograms in postseismic data processing. The blue dots represent the images in the velocity calculations. The blue lines represent generated interferograms. Note that the red dashed line indicates the date of master SAR acquisition. (a) Track 106; (b) Track 99; Figure S2: The cumulative LOS deformation from the descending observations during the 450 days after the mainshock. A, B, C, and D are the four selected points in Section 4.1; Figure S3: The logarithmic expansion of the aftershocks with time along longitude.

Author Contributions: Conceptualization, Z.T.; methodology, Y.H. and Z.T.; software, Y.H.; validation, Y.H. and Y.Z.; formal analysis, Y.H. and Z.T.; investigation, Y.H. and L.S.; resources, H.F. and W.Y.; data curation, H.F., Y.Z. and W.Y.; writing—original draft preparation, Y.H.; writing—review and editing, Z.T.; visualization, Y.H.; supervision, L.S.; project administration, H.F.; funding acquisition, Z.T. All authors have read and agreed to the published version of the manuscript.

Funding: This research was funded by National Natural Science Foundation of China, grant number 42104003, China Postdoctoral Science Foundation, grant number 2022M710012, China Postdoctoral Science Foundation, grant number 2023T160557, and State Key Laboratory of Earthquake Dynamics, China, grant number LED2022B02, the National Natural Science Foundation of China, grant number 42304004.

Institutional Review Board Statement: Not applicable.

Informed Consent Statement: Not applicable.

Data Availability Statement: The Sentinel-1 A/B precision orbit data were obtained from the European Space Agency (https://dataspace.copernicus.eu, accessed on 28 May 2024) and the archived Sentinel-1 A/B observations downloaded from the Alaska Satellite Facility (https://search.asf.alaska.edu/#/, accessed on 28 May 2024). The focal mechanism solutions (Mw $\geq$ 6) were sourced from the Global Centroid Moment Tensor Project (GCMT, https://www.globalcmt.org/CMTsearch.html, accessed on 28 May 2024).

Acknowledgments: The SDM and PSCMP/PSGRN codes were provided by Wang Rongjiang. The figures in this paper were generated using MATLAB (version 2018a) and GMT (version 6.4) software packages.

Conflicts of Interest: The authors declare no conflicts of interest.

Abbreviations

GNSS	Global Navigation Satellite System
SLC	Single Look Complex
KPJF	Kunlun Pass-Jiangcuo Fault
InSAR	Interferometric Synthetic Aperture Radar
GCMT	Global Centroid Moment Tensor Project
D-InSAR	Differential InSAR
TOPS	Terrain Observation by Progressive Scan
SRTM DEM	Shuttle Radar Topography Mission Digital Elevation Model
LOS	Line of sight
SAR	Synthetic Aperture Radar
SNR	signal-to-noise ratio
StaMPS	Stanford Method for Persistent Scatterers
PS	Persistent Scatterers
ΔCFS	Coulomb Failure Stress changes
GYXF	Garze-Yushu-Xianshuihe Fault
EKF	East Kunlun Fault
DF	Dari Fault
PS-InSAR	Persistent Scatterer InSAR

Appendix A

We adopted the Stanford Method for Persistent Scatterers (StaMPS version 4.1b) to extract the postseismic time series over the 450 days following the 2021 Maduo mainshock. Detailed StaMPS software (version 4.1b) data-processing steps are provided to ensure that this experiment can be replicated by others. We selected a multilook factor of five looks in range and one look in azimuth for the interferograms to ensure a sufficient number of candidate PS points. The slave images were registered with a single master image, and a series of interferograms were generated using the GAMMA software (version 1.0-October 2014) (Figure S1). For initial PS selection, the amplitude dispersion threshold was set to 0.4, increasing this value if few points were selected. The number of patches in range and azimuth were set to 15 and 10, respectively. The number of overlapping pixels between patches in range and azimuth was set to 100. For pixel selection, the maximum acceptable percentage of selected pixels with random phase was set to 20%. The weeded PS points were merged with a resample size of 200 m and a standard deviation threshold of 2.0 after phase correction for spatially uncorrelated look angle (SULA) error. The unwrapping method was set to ‘3D’, with the phase sampling grid set to 100 m. The phase ramp for each interferogram was estimated, and its corresponding parameter was set to 'y'. Based on the spatio-temporal characteristics of turbulence, a combination of low- and high-pass filters was adopted to effectively reduce turbulence noise. The time window and spatially correlated filtering minimum wavelength were set to 30 days and 50 m, respectively. Although StaMPS is mature software, modifying parameters can improve the accuracy of results. Therefore, the most critical factor is obtaining high-quality and abundant SAR data.

References

1. Li, Z.; Li, W.; Li, T.; Xu, Y.; Su, P.; Guo, P.; Sun, H.; Ha, G.; Chen, G.; Yuan, Z. Seismogenic fault and coseismic surface deformation of the Maduo Ms7.4 earthquake in Qinghai, China: A quick report. *Seismol. Geol.* **2021**, *43*, 722–737.
2. Pan, J.; Bai, M.; Li, C.; Liu, F.; Li, H.; Liu, D.; Chevalier, M.; Wu, K.; Wang, P.; Lu, H.; et al. Coseismic surface rupture and seismogenic structure of the 2021-05-22 Maduo (Qinghai) Ms7.4 earthquake. *Acta Geol. Sin.* **2021**, *95*, 1655–1670.
3. Liu, J.; Hu, J.; Li, Z.; Ma, Z.; Wu, L.; Jiang, W.; Feng, G.; Zhu, J. Complete three-dimensional coseismic displacements due to the 2021 Maduo earthquake in Qinghai Province, China from Sentinel-1 and ALOS-2 SAR images. *Sci. China Earth Sci.* **2022**, *65*, 687–697. [CrossRef]
4. Wang, W.; Fang, L.; Wu, J.; Tu, H.; Chen, L.; Lai, G.; Zhang, L. Aftershock sequence relocation of the 2021 Ms7.4 Maduo Earthquake, Qinghai, China. *Sci. China Earth Sci.* **2021**, *64*, 1371–1380. [CrossRef]
5. Xu, Z.; Liang, S.; Zhang, G.; Liang, J.; Zou, L.; Li, X.; Chen, Y. Analysis of seismogenic structure of Madoi, Qinghai Ms7.4 earthquake on May 22, 2021. *Chin. J. Geophys.* **2021**, *64*, 2657–2670.
6. Yang, J.; Sun, W.; Hong, S.; Yuan, Z.; Li, Y.; Chen, W.; Meng, G. Coseismic deformation analysis of the 2021 Qinghai Madoi M7.4 earthquake. *Chin. J. Geophys.* **2021**, *64*, 2671–2683.
7. Hua, J.; Zhao, D.; Shan, X.; Qu, C.; Zhang, Y.; Gong, W.; Wang, Z.; Li, C.; Li, Y.; Zhao, L.; et al. Coseismic deformation field, slip distribution and Coulomb stress disturbance of the 2021 Mw7.3 Maduo earthquake using sentinel-1 InSAR observations. *Seismol. Geol.* **2021**, *43*, 677–691.
8. Jiang, W.; Xu, C.; Li, Z.; Wu, Y.; Tan, K.; Geng, J.; Qu, C.; Zheng, G.; Wen, Y.; He, K.; et al. Using space observation techniques to study temporal and spatial characteristics of seismogenic process, occurrence and deformation of the Qinghai Madoi Mw7.4 earthquake. *Chin. J. Geophys.* **2022**, *65*, 495–508.
9. Wang, Y.; Li, Y.; Cai, Y.; Jiang, L.; Shi, H.; Jiang, Z.; Gan, W. Coseismic displacement and slip distribution of the 2021 May 22, Ms7.4 Madoi earthquake derived from GNSS observations. *Chin. J. Geophys.* **2022**, *65*, 523–536.
10. Ji, L.; Liu, C.; Xu, J.; Liu, L.; Long, F.; Zhang, Z. InSAR observation and inversion of the seismogenic fault for the 2017 Jiuzhaigou Ms7.0 earthquake in China. *Chin. J. Geophys.* **2017**, *60*, 4069–4082.
11. Zhang, G.; Qu, C.; Song, X.; Wang, C.; Shan, X.; Hu, J. Slip distribution and source parameters inverted from co-seismic deformation derived by InSAR technology of Wenchuan Mw7.9 earthquake. *Chin. J. Geophys.* **2010**, *53*, 269–279.
12. Feng, G.; Hetland, E.; Ding, X.; Zhang, L. Coseismic fault slip of the 2008 Mw 7.9 Wenchuan earthquake estimated from InSAR and GPS measurements. *Geophys. Res. Lett.* **2010**, *37*, 1302. [CrossRef]
13. Wang, K.; Fialko, Y. Observations and modeling of coseismic and postseismic deformation due to the 2015 Mw 7.8 Gorkha (Nepal) earthquake. *J. Geophys. Res. Solid Earth* **2018**, *123*, 761–779. [CrossRef]
14. Tian, Z.; Freymueller, J.; Yang, Z. Postseismic deformation due to the 2012 Mw 7.8 Haida Gwaii and 2013 Mw 7.5 Craig earthquakes and its implications for regional rheological structure. *J. Geophys. Res. Solid Earth* **2021**, *126*, e2020JB020197. [CrossRef]
15. Zheng, A.; Yu, X.; Qian, J.; Liu, X.; Zhang, W.; Chen, X.; Xu, W. Cascading rupture process of the 2021 Maduo, China earthquake revealed by the joint inversion of seismic and geodetic data. *Tectonophysics* **2023**, *849*, 229732. [CrossRef]
16. Liu, X.; Chen, Q.; Yang, Y.; Xu, Q.; Zhao, J.; Xu, L.; Liu, R. The 2021 Mw7. 4 Maduo earthquake: Coseismic slip model, triggering effect of historical earthquakes and implications for adjacent fault rupture potential. *J. Geodyn.* **2022**, *151*, 101920. [CrossRef]
17. Fang, J.; Ou, Q.; Wright, T.; Okuwaki, R.; Amey, R.; Craig, T.; Elliott, J.R.; Hooper, A.; Lazecký, M.; Maghsoudi, Y. Earthquake Cycle Deformation Associated with the 2021 Mw7.4 Maduo (Eastern Tibet) Earthquake: An Intrablock Rupture Event on a Slow-Slipping Fault From Sentinel-1 InSAR and Teleseismic Data. *J. Geophys. Res. Solid Earth* **2022**, *127*, e2022JB024268.
18. Yu, P.; Xiong, W.; Chen, W.; Qiao, X.; Wang, D.; Liu, G.; Zhao, B.; Nie, Z.; Li, Y.; Zhao, L.; et al. Slip model of the 2021 Ms7.4 Madoi earthquake constrained by GNSS and InSAR coseismic deformation. *Chin. J. Geophys.* **2022**, *65*, 509–522.
19. Wang, D.; Wang, D.; Zhao, B.; Li, Y.; Zhao, L.; Wang, Y.; Nie, Z.; Qiao, X.; Wang, Q. 2021 Qinghai Madoi Mw7.4 earthquake coseismic deformation field and fault-slip distribution using GNSS observations. *Chin. J. Geophys.* **2022**, *65*, 537–551.
20. Zhao, D.; Qu, C.; Chen, H.; Shan, X.; Song, X.; Gong, W. Tectonic and geometric control on fault kinematics of the 2021 Mw7.3 Maduo (China) earthquake inferred from interseismic, coseismic, and postseismic InSAR observations. *Geophys. Res. Lett.* **2021**, *48*, e2021GL095417.
21. Jin, Z.; Fialko, Y. Coseismic and early postseismic deformation due to the 2021 M7.4 Maduo (China) earthquake. *Geophys. Res. Lett.* **2021**, *48*, e2021GL095213.
22. He, L.; Feng, G.; Wu, X.; Lu, H.; Xu, W.; Wang, Y.; Liu, J.; Hu, J.; Li, Z. Coseismic and early postseismic slip models of the 2021 Mw 7.4 Maduo earthquake (western China) estimated by space-based geodetic data. *Geophys. Res. Lett.* **2021**, *48*, e2021GL095860.

23. Wang, S.; Song, C.; Li, S.; Li, X. Resolving co- and early post-seismic slip variations of the 2021 Mw 7.4 Madoi earthquake in east Bayan Har block with a block-wide distributed deformation mode from satellite synthetic aperture radar data. *Earth Planet. Phys.* **2022**, *6*, 108–122.
24. Zhao, L.; Xu, W.; Fang, N.; Liu, J.; Feng, G. Coseismic and early postseismic fault slip model and the seismogenic fault friction properties of the 2021 Qinghai Madoi Mw7.3 earthquake. *Chin. J. Geophys.* **2023**, *66*, 1086–1097.
25. Xiong, W.; Chen, W.; Wang, D.; Wen, Y.; Nie, Z.; Liu, G.; Wang, D.; Yu, P.; Qiao, X.; Zhao, B. Coseismic slip and early afterslip of the 2021 Mw 7.4 Maduo, China earthquake constrained by GPS and InSAR data. *Tectonophysics* **2022**, *840*, 229558. [CrossRef]
26. Chen, K.; Avouac, J.; Geng, J.; Liang, C.; Zhang, Z.; Li, Z.; Zhang, S. The 2021 Mw 7.4 Madoi earthquake: An archetype bilateral slip-pulse rupture arrested at a splay fault. *Geophys. Res. Lett.* **2022**, *49*, e2021GL095243. [CrossRef]
27. Zhao, D. Observation and Modelling of Coseismic, Postseismic and Interseismic Deformation Field of Fault Zone Using Time-Series InSAR Techniques. Ph.D. Thesis, Institute of Geology, China Earthquake Administration, Beijing, China, 2021.
28. Huang, M.; Roland, B.; Andrew, M. Probing the lithospheric rheology across the eastern margin of the Tibetan Plateau. *Earth Planet. Sci. Lett.* **2014**, *396*, 88–96. [CrossRef]
29. Song, X.; Shan, X.; Qu, C.; Han, Y.; Zhang, G.; Guo, L.; Zhang, G. The characteristics of post-seismic surface deformation of the Wenchuan Ms8.0 earthquake from InSAR. In Proceedings of the 2010 IEEE International Geoscience and Remote Sensing Symposium, Honolulu, HI, USA, 25–30 July 2010.
30. Zhao, B.; Bürgmann, R.; Wang, D.; Tan, K.; Du, R.; Zhang, R. Dominant controls of downdip afterslip and viscous relaxation on the postseismic displacements following the Mw7.9 Gorkha, Nepal, earthquake. *J. Geophys. Res. Solid Earth* **2017**, *122*, 8376–8401. [CrossRef]
31. Hong, S.; Liu, M. Postseismic Deformation and Afterslip Evolution of the 2015 Gorkha Earthquake Constrained by InSAR and GPS Observations. *J. Geophys. Res. Solid Earth* **2021**, *126*, e2020JB020230. [CrossRef]
32. Sreejith, K.; Sunil, P.; Agrawal, R.; Saji, A.; Ramesh, D.; Rajawat, A. Coseismic and early postseismic deformation due to the 25 April 2015, Mw 7.8 Gorkha, Nepal, earthquake from InSAR and GPS measurements. *Geophys. Res. Lett.* **2016**, *43*, 3160–3168. [CrossRef]
33. Qu, C.; Shan, X.; Zuo, R.; Zhang, G.; Liu, Y. An integrated study on the coseismic and post-seismic deformation of the 2010 Yushu earthquake based on InSAR analysis. *J. Earth Syst. Sci.* **2019**, *128*, 46.
34. Liu, Y.; Ji, L.; Zhu, L.; Zhang, W.; Liu, C.; Xu, J.; Li, N.; Zhang, C.; Kang, S. Postseismic deformation mechanism of the 2021 Mw7.3 Maduo earthquake, northeastern Tibetan plateau, China, revealed by Sentinel-1 SAR images. *J. Asian Earth Sci.* **2024**, *265*, 106089. [CrossRef]
35. Shu, C.; Meng, Z.; Wu, Q.; Xiong, W.; He, L.; Zhang, X.; Xu, D. Coseismic and Early Postseismic Deformation Mechanism Following the 2021 Mw 7.4 Maduo Earthquake: Insights from Satellite Radar Interferometry and GPS. *Remote Sens.* **2024**, *16*, 1399. [CrossRef]
36. Jin, Z.; Fialko, Y.; Yang, H.; Li, Y. Transient deformation excited by the 2021 M7.4 Maduo (China) earthquake: Evidence of a deep shear zone. *J. Geophys. Res. Solid Earth* **2023**, *128*, e2023JB026643. [CrossRef]
37. Wang, M.; Shen, Z. Present-day crustal deformation of continental China derived from GPS and its tectonic implications. *J. Geophys. Res. Solid Earth* **2020**, *125*, e2019JB018774. [CrossRef]
38. Wegmüller, U.; Werner, C.; Strozzi, T.; Wiesmann, A.; Frey, O.; Santoro, M. Sentinel-1 support in the GAMMA software. *Procedia Comput. Sci* **2016**, *100*, 1305–1312. [CrossRef]
39. Qu, F.; Zhang, Q.; Niu, Y.; Lu, Z.; Wang, S.; Zhao, C.; Zhu, W.; Qu, W.; Yang, C. Mapping the recent vertical crustal deformation of the Weihe Basin (China) using Sentinel-1 and ALOS-2 ScanSAR imagery. *Remote Sens.* **2022**, *14*, 3182. [CrossRef]
40. Liu, C.; Ji, L.; Zhu, L.; Zhao, C. InSAR-Constrained Interseismic Deformation and Potential Seismogenic Asperities on the Altyn Tagh Fault at 91.5–95°E, Northern Tibetan Plateau. *Remote Sens.* **2018**, *10*, 943. [CrossRef]
41. Zhu, L.; Ji, L.; Liu, C. Interseismic slip rate and locking along the Maqin-Maqu Segment of the East Kunlun Fault, Northern Tibetan Plateau, based on Sentinel-1 images. *J. Asian Earth Sci.* **2021**, *211*, 104703. [CrossRef]
42. Zhao, L.; Qu, C.; Zhao, D.; Shan, X.; Chen, H.; Liu, L. InSAR Constrained Downdip and Updip Afterslip Following the 2015 Nepal Earthquake: New Insights into Moment Budget of the Main Himalayan Thrust. *Remote Sens.* **2022**, *14*, 306. [CrossRef]
43. Tian, Z. Tectonic Deformation and Rheological Structure around the Southern Tibetan Plateau Based on the GPS Observations. Ph.D. Thesis, Chang'an University, Xi'an, China, 2020.
44. Hooper, A. Persistent Scatter Radar Interferometry for Crustal Deformation Studies and Modeling of Volcanic Deformation. Ph.D. Thesis, Stanford University, Stanford, CA, USA, 2006.
45. Ferretti, A.; Prati, C.; Rocca, F. Permanent scatterers in SAR interferometry. *IEEE Trans. Geosci. Remote Sens.* **2001**, *39*, 8–20. [CrossRef]
46. Ding, X.; Li, Z.; Zhu, J.; Feng, G.; Long, J. Atmospheric effects on InSAR measurements and their mitigation. *Sensors* **2008**, *8*, 5426–5448. [CrossRef] [PubMed]
47. Parker, A.; Biggs, J.; Walters, R.; Ebmeier, S.; Wright, T.; Teanby, N.; Lu, Z. Systematic assessment of atmospheric uncertainties for InSAR data at volcanic arcs using large-scale atmospheric models: Application to the Cascade volcanoes, United States. *Remote Sens. Environ.* **2015**, *170*, 102–114. [CrossRef]
48. Okada, Y. Surface deformation due to shear and tensile faults in a half-space. *Bull. Seismol. Soc. Am.* **1985**, *75*, 1135–1154. [CrossRef]

49. Wang, R.; Diao, F.; Hoechner, A. SDM-A geodetic inversion code incorporating with layered crust structure and curved fault geometry. In Proceedings of the EGU General Assembly Conference Abstracts, Vienna, Austria, 7–12 April 2013; Volume 15, p. EGU2013-2411-1.
50. Guo, R.; Yang, H.; Li, Y.; Zheng, Y.; Zhang, L. Complex slip distribution of the 2021 Mw 7.4 Maduo, China, Earthquake: An event occurring on the slowly slipping fault. *Seismol. Res. Lett.* **2021**, *93*, 653–665. [CrossRef]
51. Su, L. The Analysis and Mechanism Research of Postseismic Deformation Based on GPS Coordinate Time Series. Ph.D. Thesis, Institute of Geology, China Earthquake Administration, Beijing, China, 2020.
52. Tian, Z.; Freymueller, J.; Yang, Z.; Li, Z.; Sun, H. Frictional properties and rheological structure at the Ecuadorian subduction zone revealed by the postseismic deformation due to the 2016 Mw7.8 Pedernales (Ecuador) earthquake. *J. Geophys. Res. Solid Earth* **2023**, *128*, e2022JB025043. [CrossRef]
53. Liu, X.; Xu, W. Logarithmic model joint inversion method for coseismic and postseismic slip: Application to the 2017 Mw 7.3 Sarpol Zahāb earthquake, Iran. *J. Geophys. Res. Solid Earth* **2019**, *124*, 12034–12052. [CrossRef]
54. Agurto, H.; Rietbrock, A.; Ryder, I.; Miller, M. Seismic-afterslip characterization of the 2010 Mw 8.8 Maule, Chile, earthquake based on moment tensor inversion. *Geophys. Res. Lett.* **2012**, *39*, L20303. [CrossRef]
55. Agurto, H.; Font, Y.; Charvis, P.; Régnier, M.; Rietbrock, A.; Ambrois, D.; Paulatto, M.; Alvarado, A.; Beck, S.; Courboulex, F.; et al. Ridge subduction and afterslip control aftershock distribution of the 2016 Mw 7.8 Ecuador earthquake. *Earth Planet. Sci. Lett.* **2019**, *520*, 63–76. [CrossRef]
56. Harris, R. Introduction to special section: Stress triggers, stress shadows, and implications for seismic hazard. *J. Geophys. Res.* **1998**, *103*, 24347–24358. [CrossRef]
57. Li, Y.; Huang, L.; Ding, R.; Yang, S.; Liu, L.; Zhang, S.; Liu, H. Coulomb stress changes associated with the M7.3 Maduo earthquake and implications for seismic hazards. *Nat. Hazards Res.* **2021**, *1*, 95–101. [CrossRef]
58. Zhu, A.; Wang, Y.; Li, Y.; Zhang, D. Numerical simulation on the mechanism of the Madoi, Qinghai Ms 7.4 earthquake constrained by InSAR deformation. *Chin. J. Geophys.* **2021**, *64*, 4548–4561.
59. Li, C. The Long-Term Faulting Behavior of the Eastern Segment (Maqin-Maqu) of the East Kunlun Fault Since the Late Quaternary. Ph.D. Thesis, Institute of Geology, China Earthquake Administration, Beijing, China, 2009.
60. Shan, B.; Xiong, X.; Wang, R.; Zheng, Y.; Yadav, R. Stress evolution and seismic hazard on the Maqin-Maqu segment of East Kunlun Fault zone from co-, post and interseismic stress changes. *Geophys. J. Int.* **2015**, *200*, 244–253. [CrossRef]